Research Square

Preprints are preliminary reports that have not undergone peer review.
They should not be considered conclusive, used to inform clinical practice,
or referenced by the media as validated information.

Electrical signatures accompanying phototropic growth in Aloe vera: a long-term case study

Panagiotis Mougkogiannis

pmougoyannis@gmail.com

University of the West of England

Andrew Adamatzky

University of the West of England

Research Article

Keywords: Plant electrophysiology, Diurnal rhythm, Electrochemical impedance spectroscopy, Crassulacean acid metabolism

Posted Date: November 16th, 2026

DOI: https://doi.org/10.21203/rs.3.rs-11580844/v1

License: This work is licensed under a Creative Commons Attribution 4.0 International License.
Read Full License

Additional Declarations: No competing interests reported.

Electrical signatures accompanying phototropic growth in *Aloe vera*: a long-term case study

Panagiotis Mougkogiannis[1*] and Andrew Adamatzky[1]

[1*]Unconventional Computing Laboratory, University of the West of England, Bristol, United Kingdom.

*Corresponding author(s). E-mail(s): pmougoyannis@gmail.com;
Contributing authors: andrew.adamatzky@uwe.ac.uk;

Abstract

Plant electrical activity spans seconds to weeks, but long recordings that also assess electrode polarization are rare. We recorded extracellular potentials from a potted *Aloe vera* L. plant for 37 days with eight differential Pt/Ir channels sampled at 1 Hz (3 198 387 samples per channel), while the plant visibly bent and grew towards a window. After about one week of electrode settling, all channels showed a rhythm of 1 cycle day^{-1}, 5–58 times above background. The largest, on V_7, spanned 65 mV, rising at 06:15 and falling at 20:00 UTC, and contained 107 abrupt steps, 89 of them negative and concentrated in the evening. Over four weeks, both V_7 plateaus drifted upwards at 5.2 mV/d ($r = 0.97$) with a stable daily amplitude, and V_6 showed a logistic rise of 25.3 mV (width 1.3 d). Outdoor reanalysis data for Patras showed that the V_7 waveform followed air temperature ($r = 0.76$) but lagged its evening decline by 2.5 h. Hour-to-hour weather anomalies did not explain the signals, the daily amplitude was smaller on hot, dry days, and no weather trend matched the drift. Impedance spectra (0.1 Hz–100 kHz) from a three-electrode configuration with printed Au and Pt/Ir electrodes gave a tissue resistance of 270 kΩ in parallel with a constant-phase element ($n = 0.82$, 2.9 nF), consistent with differential pulse and cyclic voltammetry. Environmental SEM showed a waxy cuticle and sunken stomata. A Boolean analysis identified a 2.2 V threshold switch, while an apparent $V_7 = L$ AND NOT V_5 relation reduced to $V_7 = \mathbf{NOT}\, V_5$ with independent day/night inputs.

Keywords: Plant electrophysiology, Diurnal rhythm, Electrochemical impedance spectroscopy, Crassulacean acid metabolism

1 Introduction

Higher plants generate action, variation and system potentials. These signals connect environmental stimuli with photosynthesis, gas exchange and growth [1–4]. Simple electrodes can detect this activity. Plants have therefore been proposed as living environmental biosensors [5, 6]. Their use requires long recordings that distinguish physiological rhythms from electrode artefacts.

Aloe vera L. provides a useful system for such measurements. This succulent uses crassulacean acid metabolism (CAM). Its stomata open at night, when CO_2 is stored as vacuolar malic acid. CO_2 is then released for photosynthesis during the light period [7]. This cycle produces daily changes in proton and ion fluxes. The large, water-rich leaves also permit electrochemical measurements. Volkov and co-workers reported anisotropic and nonlinear electrical circuits in *Aloe* leaves [8]. They also identified day/night changes in electrical properties [9] and memristive elements in the leaf network [10]. Impedance spectroscopy complements these observations. It describes plant tissues through equivalent circuits associated with membranes, the apoplast and the symplast [11, 12].

Daily electrical rhythms occur alongside slower changes in plant form. Phototropism directs shoot growth towards light. Blue-light photoreceptors and auxin redistribution promote differential cell elongation [13, 14]. In a large succulent, visible reorientation can extend over days. Electrical recordings across this process remain scarce.

Here, we examine an unplanned observation during a five-week recording. The plant visibly turned and grew towards a window [Fig. 1]. We analyse all eight channels at 1-s resolution and relate their temporal structure to subsequent electrochemical measurements. The analysis separates daily rhythms, abrupt steps and slow baseline changes. Impedance and voltammetry then characterize the plant–electrode system. Together, these measurements establish an electrical description of a reorienting plant without assigning a causal role to phototropism.

2 Materials and methods

2.1 Plant and electrodes

A mature *Aloe vera* L. plant grew in a metal pot [Fig. 1]. It was kept indoors on a tiled floor beside a window. The window provided the only directional light source. Platinum–iridium (Pt/Ir) wires were inserted through the lamina at several positions on different leaves. Sixteen electrodes formed eight differential pairs (1–2, 3–4, …, 15–16). Each pair recorded a voltage V_k, where $k = 1, \ldots, 8$.

The plant was kept in Patras, Greece (38.28°N, 21.77°E). Two environmental events were annotated during recording. The plant was watered once, on 21 July 2025 at 08:00:56 UTC (“water in”). Strong wind was noted on 9 August 2025 at 03:55 UTC.

2.2 Long-term potential recording

Potentials were recorded with a 24-bit PicoLog ADC-24 logger (serial JO325/095). The logger operated in differential mode over ±2.5 V and was controlled by PicoLog 6



Fig. 1 The *Aloe vera* plant with wire electrodes inserted in the leaves. Cables connect the electrodes to the data logger (right). During recording, the rosette bent and grew towards the window.

(v6.2.13). Each channel was sampled at 1 s intervals in “average” mode. Each stored value therefore represents the mean of the conversions within that second.

Recording began on 14 July 2025 at 09:43:33 UTC and ended on 20 August 2025 at 10:31:05 UTC. The duration was 37.03 d, with 3 198 387 samples per channel and 25.6×10^6 samples in total. A single 1266 s gap occurred on day 2.6. We filled this gap by linear interpolation. Analyses use the native 1-s data unless stated otherwise. Times are reported in UTC as stored by the logger, whose clock was set to Europe/London.

2.3 Electrochemical measurements

Electrochemical measurements followed the potential recording. We used a PalmSens4 potentiostat (serial PS4A23G004794; PSTrace 5.9) in a three-electrode configuration. The cell combined printed gold (Au) electrodes with Pt/Ir electrodes in a leaf. Potentials are reported against the reference electrode of this configuration. Below, "Au–tissue system" denotes this electrode set with the printed Au electrode in contact with the tissue. Measurements were performed on 31 August and 1 September 2025. Start times below are in UTC.

1. *Galvanostatic impedance tracking (GEIS)* began on 31 August at 19:25. Frequency was fixed at 1 kHz, with zero DC current. The session lasted 20 000 s. It contained 17 025 points with a median spacing of 1.18 s.
2. *Potentiostatic EIS* began on 1 September at 18:15 and 18:37. Each spectrum used 58 logarithmically spaced frequencies from 1 MHz to 0.1 Hz. The DC potential was $E_{\mathrm{dc}} = 0.1\,\mathrm{V}$. Sinusoidal amplitudes were 10 mV and 100 mV.
3. *EIS potential scanning* began on 1 September at 18:19. The same frequency grid was used at six DC potentials: $E_{\mathrm{dc}} = 0.1, 0.3, \ldots, 1.1\,\mathrm{V}$. The amplitude was 10 mV.
4. *DPV* was performed on 1 September from 18:42 to 20:09. Scans covered -4 to 4 V, with a 10 mV step. Pulse time was 0.3 s and scan rate was 10 mV/s. Pulse amplitudes were $\Delta E_{\mathrm{p}} = 0.1$, 0.2, 0.3, 0.5, 0.7 and 0.9 V.
5. *CV* began on 1 September at 20:11. Twenty cycles were recorded between -1 and 1 V. The scan rate was $\nu = 10\,\mathrm{mV/s}$ and the step was 10 mV.

Raw session files were parsed directly from PalmSens Potentiostat. All recorded points were retained.

Boolean-logic analysis. We examined three possible Boolean descriptions of the electrical measurements.

First, each DPV curve was treated as a transfer function. Applied potential served as the input and differential current as the output. The "0" level was the median current for $|E| < 1.5\,\mathrm{V}$. The "1" level was the median for $2.5 < |E| < 3.8\,\mathrm{V}$. The switching threshold was the potential at the midpoint between these levels. We calculated the ON/OFF ratio and the fraction of points classified correctly by this midpoint. Level separation was quantified by $d' = (\mu_1 - \mu_0)/\sqrt{(\sigma_1^2 + \sigma_0^2)/2}$.

Second, we examined CV hysteresis. A loop pinched at the origin is a characteristic signature of a memristive element [10, 19]. We located crossings between the forward and backward branches of each cycle. We also calculated the loop area, $\oint I\,\mathrm{d}E$.

Third, we searched for Boolean relations between recording channels. Settled-period data were averaged into 4324 bins of 10 min. A channel was assigned 1 above its 24-h running median and 0 otherwise. This procedure suppresses slow drift while retaining the day/night state. A day/night proxy, L, was assigned 1 from 06:15 to 20:00 UTC and 0 otherwise. These boundaries were the half-amplitude times of V_7; L was not an independent light measurement.

For each output y, inputs were drawn from $\{L, V_1, \ldots, V_8\} \setminus \{y\}$. We tested all 16 two-input Boolean functions for each of the 28 input pairs. The most accurate function was compared with the best single-input COPY or NOT function. Significance was assessed using 1000 circular shifts of y. Shifts were at least 3 days, with an additional

offset of 3–21 h. Circular shifting retains autocorrelation and periodic structure while changing alignment with the inputs. The full search over input pairs was repeated for every shifted series.

2.4 Meteorological data

Hourly outdoor air temperature at 2 m, relative humidity (RH), shortwave solar radiation, cloud cover and wind gusts at 10 m were obtained for Patras (38.28°N, 21.77°E, 13 m elevation) from the Open-Meteo historical archive [22], which is based on the ERA5 reanalysis [21]. Radiation is the mean over the preceding hour and was assigned to the middle of that hour. Sunrise, solar noon and sunset were calculated for the site. These outdoor values are a proxy: indoor temperature and humidity at the plant were not measured.

Channel potentials were averaged into hourly means and aligned with the weather series for the settled period (721 h). Three analyses were made. (i) *Phase.* After removing a 24-h running mean from each series, we computed lagged correlations for lags of ±8 h and compared mean daily profiles. (ii) *Anomalies.* We also removed the mean profile for each hour of the day. The remaining hour-to-hour anomalies of each channel were regressed on temperature and radiation anomalies, with heteroscedasticity- and autocorrelation-consistent (HAC, 24-h) standard errors. This tests whether weather deviations, rather than the shared daily cycle, drive the potentials. (iii) *Daily scale.* For 22 July–19 August (29 days), the daily amplitude and the detrended day and night plateaus of V_7 were correlated with daily mean temperature, maximum temperature, temperature range, mean RH and total radiation. For the Boolean analysis, three independent day/night inputs were also defined in 10-min bins: radiation above 50 W/m^2, temperature above its 24-h running median, and RH below its 24-h running median.

2.5 Scanning electron microscopy

Leaf surfaces were examined by environmental scanning electron microscopy. Images were acquired with a gaseous secondary-electron detector (GSED). Uncoated specimens were imaged on 1 September 2025 at 10 kV. The chamber contained water vapour at 5 Torr, allowing imaging without a conductive coating.

Gold-sputtered specimens were imaged on 3 September 2025 at 7.65 kV and 2 Torr. The spot size was 3.0 in both sessions. Working distances were 5.8–6.8 mm for uncoated specimens and 8.3 mm for coated specimens. Feature dimensions were calculated from the horizontal field width recorded in each image.

A further Au-coated specimen was imaged on 5 September 2025 in high vacuum (1.95×10^{-5} Torr) with an Everhart–Thornley detector (ETD) at 2.00 kV, spot size 3.0, a working distance of 10.2 mm and a horizontal field width of 1.52 mm (0.99 µm per pixel). Stomata in this field were located as dark, compact pits with a background-subtracted intensity threshold (41-pixel median background) and size limits, and each candidate was inspected visually. Candidates on cracks, in a deep groove or cut by the image edge were rejected. The density confidence interval was taken from the Poisson distribution. Spatial regularity was tested with the Clark–Evans nearest-neighbour ratio, using Donnelly's edge correction for the expected distance [23, 24].

Spikes and the stomatal phase. *Aloe vera* opens its stomata mainly at night (CAM phase I) [7]. We therefore asked whether the step events ("spikes") of the settled period clustered in the night, defined from the calculated sunset and sunrise at Patras. The night fraction of the record served as the null probability in a binomial test. For V_7, events were also counted for each night (sunset to next sunrise, 21 July–19 August, 30 nights) and related to the mean night air temperature, RH and vapour-pressure deficit (VPD) from the Open-Meteo data. Rank correlations and negative-binomial regression were used because the counts were overdispersed (Poisson dispersion 2.1).

2.6 Data analysis

Noise. The white-noise floor was estimated from first differences, $\delta V_i = V_{i+1} - V_i$. We used $\sigma_{\mathrm{n}} = 1.4826\,\mathrm{MAD}(\delta V)/\sqrt{2}$. This estimator is insensitive to slow trends.

Spectra. Power spectral densities (PSDs) were calculated with Welch's method for the settled period, from day 7 onwards [15]. Each segment was detrended linearly. For 0.1–700 cycles/d, we used 8-day segments of 1-min means. For 3×10^{-4}–0.5 Hz, we used 1-h segments of the 1-s data. Diurnal strength was defined as the PSD at 1 cycle day^{-1} divided by the median PSD from 0.6 to 3 cycles day^{-1}.

Diurnal analysis. For each UTC day, the night plateau was the median from 00:00 to 04:00. The day plateau was the median from 10:00 to 16:00. Their difference defined the daily amplitude. To obtain mean daily profiles, we first removed each day's mean. The 1-s data were then folded into 15-min bins by time of day.

Step transitions. Each channel was filtered with a fourth-order, zero-phase Butterworth low-pass filter at 0.03 Hz. We then calculated the 30 s increment, $\Delta_{30}V(t) = V(t + 30\,\mathrm{s}) - V(t)$. Events were clusters with $|\Delta_{30}V| > 10\,\mathrm{mV}$. Samples separated by less than 10 min were merged. The extreme increment was retained for each event.

Slow transitions were fitted with a logistic function

$$V(t) = V_0 + \frac{A}{1 + \exp[-(t - t_0)/w]}, \tag{1}$$

where w sets the transition width. The 10–90% rise time is $2w \ln 9 \approx 4.39\,w$.

Impedance model. Spectra were fitted with

$$Z(\omega) = \left[R_1^{-1} + Q_1(\mathrm{j}\omega)^{n_1}\right]^{-1} + \left[Q_2(\mathrm{j}\omega)^{n_2}\right]^{-1}, \tag{2}$$

Here, R_1 represents ionic tissue resistance. The constant-phase element (CPE) (Q_1, n_1) describes distributed membrane/tissue capacitance. The second CPE, (Q_2, n_2), describes electrode–tissue polarization [16]. The effective capacitance of the parallel R_1–CPE$_1$ element was calculated using Brug's formula [17]. The corresponding expressions are

$$C_{\mathrm{eff}} = \frac{(Q_1 R_1)^{1/n_1}}{R_1}, \qquad f_{\mathrm{c}} = \frac{1}{2\pi (R_1 Q_1)^{1/n_1}}. \tag{3}$$

Fitting jointly minimized the least-squares residuals of $\ln|Z|$ and phase. The fitted band was 0.1 Hz–110 kHz. Points from 30 to 60 Hz were excluded because of

Table 1 Channel statistics for the settled period (day 7 to end). $\tilde{V}$: median; s: standard deviation; σ_{n}: white-noise floor (whole record); V_{pp}: peak-to-peak value of the mean daily profile; P_1: PSD ratio at 1 cycle day^{-1}; N_{s}: step events with $|\Delta_{30}V| > 10\,\mathrm{mV}$.

Ch.	$\tilde{V}$ (mV)	s (mV)	σ_{n} (mV)	V_{pp} (mV)	P_1	N_{s}
V_1	−2.1	7.1	0.11	1.8	50	2
V_2	0.2	3.5	0.33	0.6	7	0
V_3	−7.0	5.6	0.20	2.2	29	1
V_4	1.4	10.9	0.35	5.4	27	35
V_5	5.4	3.6	0.13	3.3	36	1
V_6	4.0	12.6	1.23	1.5	15	33
V_7	−106.8	58.5	0.42	65.2	58	107
V_8	0.4	2.6	0.09	1.1	5	1

mains interference. Points from 0.6 to 2.1 kHz were also excluded because current-range switching produced outliers [open symbols in Fig. 7]. Above 200 kHz, the real impedance became negative. We attributed this behaviour to cable and instrument parasitics and excluded those points. An added series resistance converged to zero. It could not be resolved and was omitted.

CV and DPV. Forward and backward CV branches were interpolated onto a common potential grid. Their mean defined the chord conductance, $G = \mathrm{d}I/\mathrm{d}E$, and the zero-current potential, E_0. The branch separation near $E \approx 0$ gave $C_{\mathrm{CV}} = \Delta I/(2\nu)$ [18]. For DPV, we calculated the median differential current in three windows: $-3.8 < E < -2.2$ V, $|E| < 1.5$ V and $2.5 < E < 3.8$ V. An ohmic element obeys $\Delta I = \Delta E_{\mathrm{p}}/R$. The slope of ΔI against pulse amplitude therefore gives the resistance in each window.

3 Results

3.1 Overview and electrode settling

Figure 2 shows the complete eight-channel recording as 1-min means. During the first week, excursions reached ±200 mV. The signals then approached quasi-stable levels. Three channels relaxed approximately exponentially: V_2 ($\tau = 23$ h, $R^2 = 0.87$), V_5 (1.7 h, $R^2 = 0.83$) and V_6 (135 h, $R^2 = 0.74$). We attribute this initial phase mainly to wound healing and equilibration at the inserted electrodes. Day 7 onwards was therefore treated as the settled period.

After this initial relaxation, the channels retained distinct temporal patterns. Table 1 summarizes their statistics. The estimated white-noise floor was 0.09–0.42 mV on seven channels. It was higher on V_6, at 1.2 mV.

3.2 Diurnal rhythm

The settled signals shared a daily rhythm. All channels showed a peak at 1 cycle day^{-1} [Fig. 6(a)]. Peak power was 5–58 times above background (Table 1). The second harmonic was weak, with a PSD ratio of ≤ 2.7.

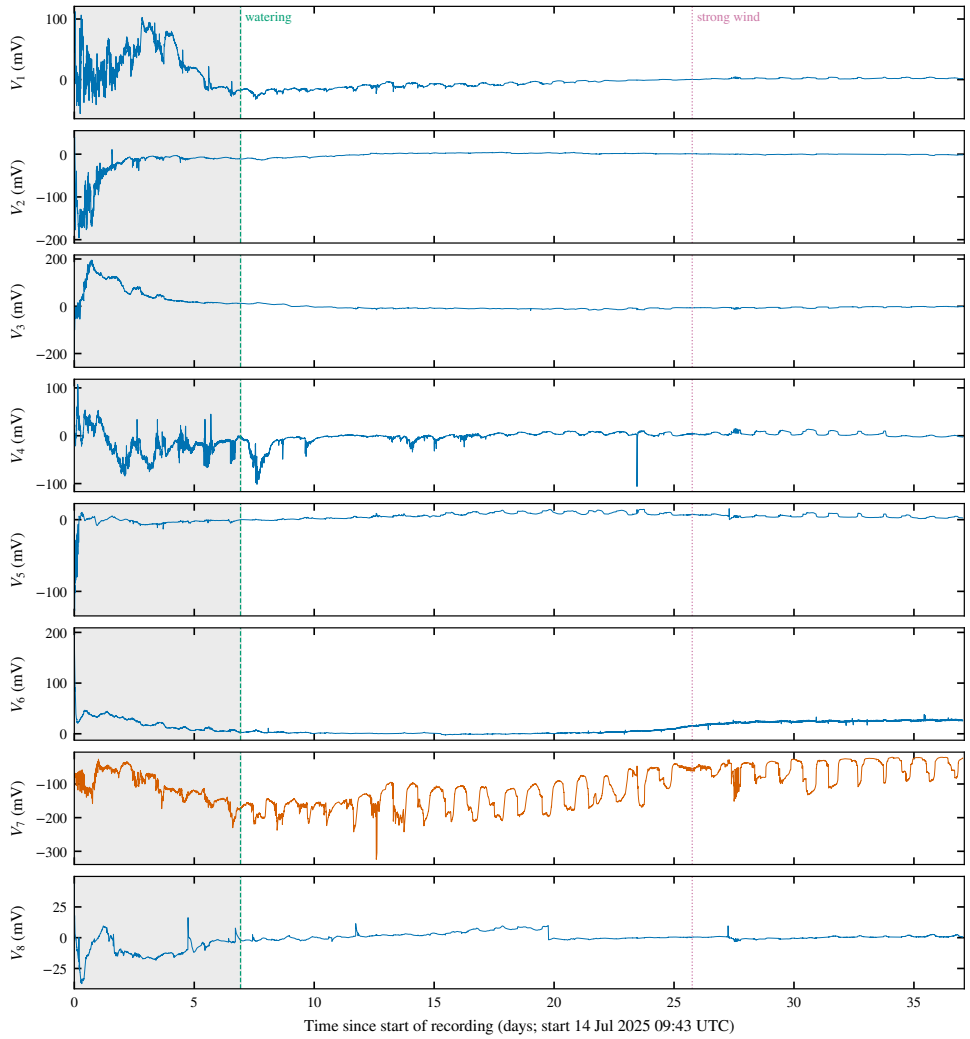


Fig. 2 All eight differential potentials V_1–V_8 over the full 37-day recording (1-min means of the 1-s data). Grey band: electrode-settling period (days 0–7). Dashed line: watering (21 Jul., 08:01 UTC). Dotted line: strong wind (9 Aug., 03:55 UTC). V_7 (orange) carries the dominant day/night rhythm.

The largest rhythm occurred on V_7 [Fig. 3]. Its mean daily profile resembled a rounded square wave and spanned 65.2 mV. The minimum occurred at 03:30 UTC. The signal crossed its half-amplitude level at 06:15, remained approximately flat from 09:00 to 16:00 and crossed downwards at 20:00 UTC [Fig. 3(c)]. The rhythm was also evident in the raw 1-s data [Fig. 3(a)]. It was therefore not produced by a few isolated events.

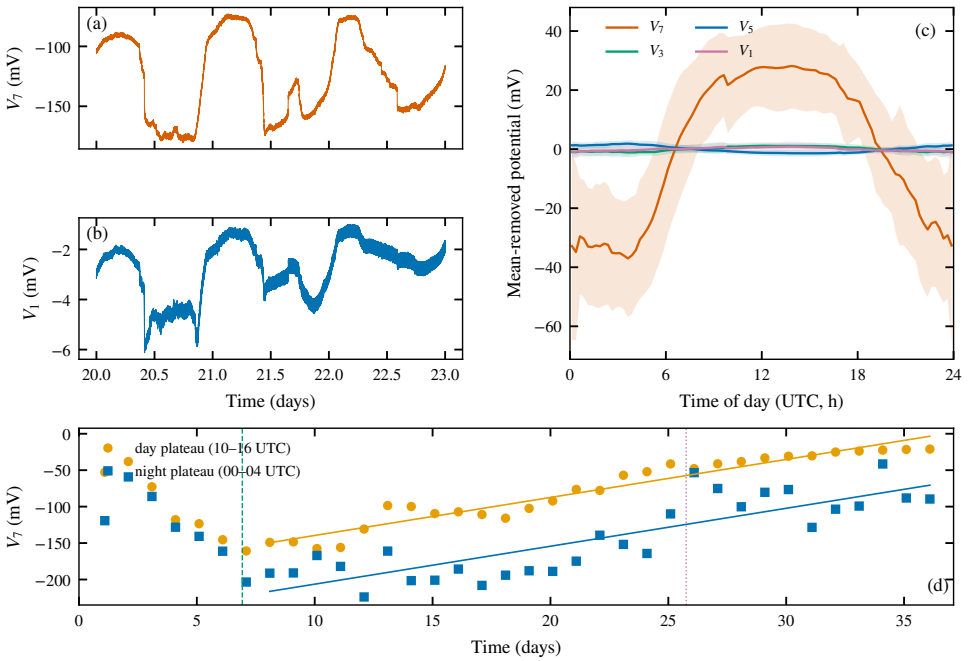


Fig. 3 Diurnal behaviour. (a,b) Raw 1-s data for V_7 and V_1 over days 20–23. (c) Mean daily profiles of V_7, V_3, V_5 and V_1. Profiles use 15-min bins from day 7 onwards, with each day's mean removed. The band shows ±1 standard deviation across days for V_7. (d) Daily day (10–16 UTC) and night (00–04 UTC) plateaus of V_7. Linear fits from 22 July onwards have slopes of 5.22 and 5.20 mV/d. Dashed and dotted lines mark watering and strong wind.

Smaller rhythms were phase-locked to V_7. Channels V_3 (2.2 mV) and V_1 (1.8 mV) were in phase. Channels V_4 (5.4 mV) and V_5 (3.3 mV) were in antiphase. Hourly increments supported this pattern: $r(V_7, V_3) = 0.77$, $r(V_7, V_5) = -0.81$, $r(V_3, V_5) = -0.78$ and $r(V_7, V_1) = 0.55$. By comparison, V_2, V_6 and V_8 showed weak correlations with the other channels ($|r| < 0.3$). Fluctuations in V_1 also followed V_7 at sub-hour scales [Fig. 3(a,b)].

3.3 Step transitions

The daily waveform contained abrupt transitions. During the settled period, V_7 showed 107 events with $|\Delta_{30}V| > 10$ mV [Fig. 4(a)]. Of these, 89 were negative. Their median magnitude was 21.4 mV over 30 s. Most negative events (86) occurred between 15:00 and 03:00 UTC. They therefore clustered during the evening decline and early night. The 18 positive steps had a median magnitude of 25.6 mV. Their timing was more dispersed, although 8 occurred between 03:00 and 09:00.

Several large steps were followed by partial recovery over tens of minutes [Fig. 3(a)]. On 10–11 August, V_7 showed four drop–recovery pairs of 70–113 mV. Intervals between them were 0.7–1.1 h. Comparable events occurred on V_4 (35) and V_6 (33). Each remaining channel showed at most two. Discrete events thus contributed to the evening

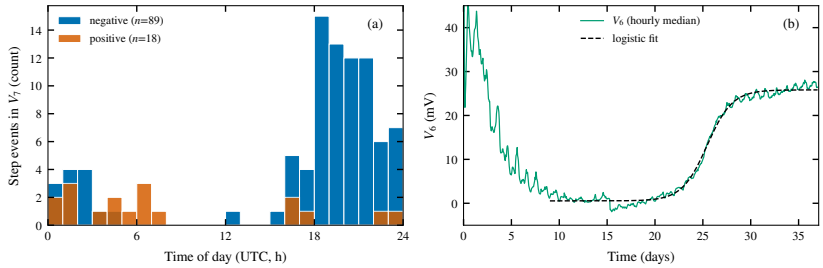


Fig. 4 (a) Time-of-day histogram of the step transitions of V_7 ($|\Delta_{30}V| > 10\,\mathrm{mV}$, day 7 onward). (b) Hourly median of V_6 with the logistic fit of Eq. (1) (fit range: day 9 onward).

decline. Their time scale resembles that of variation potentials, although timing alone does not identify the signal type [2, 3].

3.4 Slow drifts and a logistic transition

Abrupt events were superimposed on a much slower baseline change. From 22 July to 19 August, the daily amplitude of V_7 showed no trend ($(0.01 \pm 0.66)\,\mathrm{mV/d}$, $p = 0.99$). Both plateaus nevertheless drifted upwards [Fig. 3(d)]. The daytime slope was $5.22\,\mathrm{mV/d}$ ($r = 0.97$, $p = 2.5 \times 10^{-17}$). The night-time slope was $5.20\,\mathrm{mV/d}$ ($r = 0.84$, $p = 1.5 \times 10^{-8}$). Over 28 days, the day plateau moved from approximately -149 to $-21\,\mathrm{mV}$. The similar slopes indicate a baseline shift with little change in daily amplitude. This pattern is consistent with a slow contribution added to the rhythmic source.

Channel V_6 showed a distinct slow transition [Fig. 4(b)]. It approached 0 mV during days 10–20, then rose in a single sigmoidal step. The fitted amplitude was $A = (25.28 \pm 0.09)\,\mathrm{mV}$. The midpoint was $t_0 = (25.45 \pm 0.02)\,\mathrm{d}$, corresponding to 8 August 2025 at 20:27 UTC. The width was $w = (1.31 \pm 0.02)\,\mathrm{d}$, giving a 10–90% rise time of 5.8 d. The logistic fit gave $R^2 = 0.993$ [Eq. (1)]. The signal remained at its new level until recording ended. Noise and step activity also increased after the transition (Fig. 2).

3.5 Responses to watering and wind

The annotated events provide limited context for these changes. Watering occurred at 08:01 UTC, during the morning rise of V_7. From 08:00 to 14:00 that day, V_7 increased by 19.1 mV. This was within the variation over the same interval on other days ($18.3 \pm 22.1\,\mathrm{mV}$, $z = 0.03$). The largest deviation on V_4 was $-12\,\mathrm{mV}$, 94 min after watering. Its 6-h change was also within the day-to-day spread ($z = -0.75$). No immediate response to watering was therefore resolved.

The daily amplitude of V_7 increased over a longer interval. It rose from $15.6 \pm 3.6\,\mathrm{mV}$ on 16–20 July to $42.5 \pm 0.2\,\mathrm{mV}$ on 21–23 July. It reached $72.8 \pm 26.2\,\mathrm{mV}$ over 26 July–19 August. This pattern is compatible with recovery after rehydration. However, it overlaps with electrode settling, so the two contributions cannot be separated.

The wind annotation coincided with a shorter disturbance. At 03:55 UTC on 9 August, V_7 dipped by 7.4 mV within 5 min. The following daily cycle was the weakest

in the settled record, with an amplitude of 5.6 mV. Its night plateau was unusually high, at −53 mV. The amplitude recovered to 33.9 mV on 10 August. Mechanical stimulation, altered light exposure and temperature changes remain possible explanations. The weather data in the next section place this event during a windy, warm and dry period.

3.6 Weather and temperature correlations

Outdoor conditions in Patras were hot and dry for most of the record (Fig. 5). Hourly air temperature ranged from 21.4 to 40.4 °C (mean 28.8 °C), and RH from 17 to 89% (mean 49%). Daily maxima ranged from 28.4 °C (5 August) to 40.4 °C (25 July). Air temperature and RH were strongly anticorrelated ($r = -0.87$ for hourly values after removing the 24-h mean), so their effects cannot be separated. Daily mean temperature showed no trend over the settled period (−0.05 K day^{-1}, $p = 0.41$), and RH showed no significant trend (−0.47% day^{-1}, $p = 0.13$).

Phase of the daily cycle. Over the period, sunrise moved from 03:20 to 03:51 UTC, solar noon was near 10:38 UTC, and sunset moved from 17:57 to 17:22 UTC. The mean V_7 profile followed air temperature more closely than radiation [Fig. 5(a)]. Its morning rise coincided with the rise in radiation, temperature and the fall in RH, with half-amplitude crossings within about 0.5 h of each other near 06:00–06:30 UTC. Its maximum (about 13:30 UTC) was close to that of air temperature (about 13:00 UTC), but it fell through half amplitude near 20:00 UTC. This is about 2.5 h after air temperature, 1.5 h after RH and 4.5 h after radiation. In hourly correlations, V_7 correlated best with air temperature at zero lag ($r = 0.76$), with RH at zero lag ($r = -0.74$) and with radiation at a lag of 1 h ($r = 0.73$). The antiphase channel V_5 lagged by 1–3 h ($r = -0.68$ with temperature, $r = -0.65$ with radiation), and V_3 showed weaker in-phase relations ($r = 0.42$ with temperature).

Hour-to-hour anomalies. Once the mean daily cycle was removed, weather anomalies explained almost none of the channel variance. All channels had $|r| \leq 0.23$ with anomalies of temperature, RH or radiation, and $R^2 \leq 0.06$ in the joint regressions. For V_7, the temperature coefficient was -2.4 ± 1.6 mV/K ($p = 0.13$). Only V_1 had a significant radiation coefficient (1.5 mV per 100 W/m^2, $p < 0.001$). Thus, the potentials follow the shape of the average day but not the weather fluctuations within individual days. This is expected if the plant responds mainly to the daily light and indoor thermal cycle, which is buffered relative to outdoor weather.

Daily scale. Day-to-day variation was more informative. The daily amplitude of V_7 was smaller on hotter, drier days: $r = -0.44$ with mean temperature ($p = 0.017$), $r = -0.45$ with maximum temperature ($p = 0.014$) and $r = +0.46$ with mean RH ($p = 0.012$) [Fig. 5(b)]. The detrended day plateau was unrelated to the weather ($|r| \leq 0.21$). The change came from the night plateau, which was less negative on warm, dry days ($r = +0.45$ with mean temperature, $p = 0.014$; $r = -0.50$ with RH, $p = 0.006$). Warm, dry nights therefore compressed the daily cycle from below. With 29 days and autocorrelated weather, these values are descriptive.

Two events can be placed in this context. The heat peak of 25–26 July (maxima of 40.4 and 40.3 °C, mean RH about 30%) did not produce a distinct step in any channel. The logistic rise of V_6 (midpoint 8 August, 20:27 UTC) coincided with the

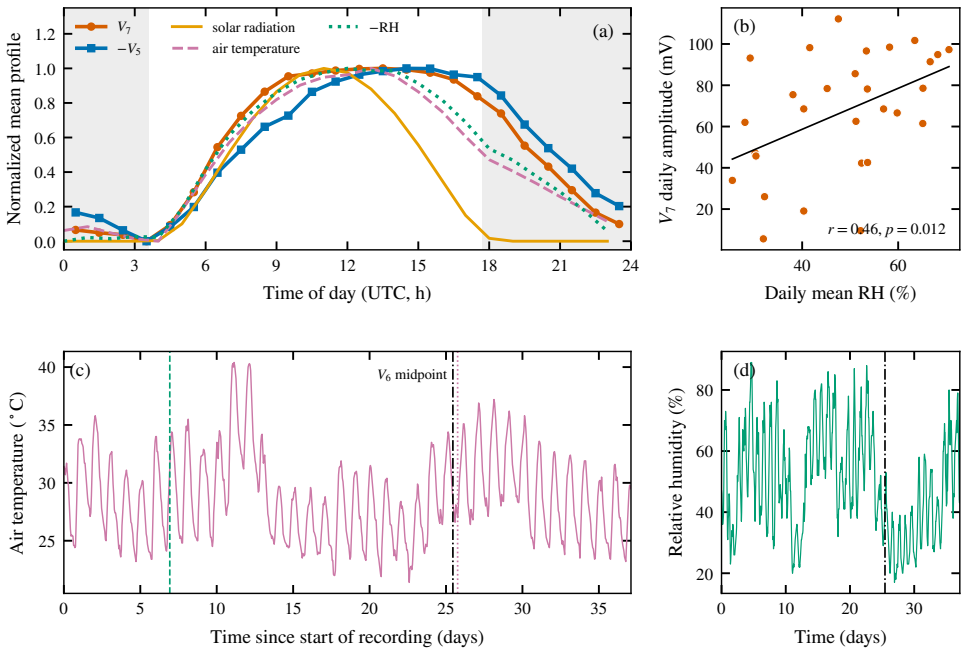


Fig. 5 Outdoor weather in Patras (Open-Meteo/ERA5) and the potentials. (a) Normalized mean daily profiles (settled period) of V_7, inverted V_5, solar radiation, air temperature and inverted RH; grey bands mark night between mean sunset and sunrise. (b) Daily amplitude of V_7 against daily mean RH (22 July–19 August), with a linear fit. (c) Hourly air temperature and (d) RH over the recording. Dashed line: watering; dotted line: wind annotation; dash-dotted line: midpoint of the V_6 logistic transition.

onset of a warm, dry spell. Mean RH fell from 68% on 6 August to 26–32% on 9–12 August, and mean temperature rose from 25.9 to 31.5 °C [Fig. 5(c,d)]. A single coincidence cannot establish a cause, but it makes leaf water status a candidate alongside mechanical rearrangement. Gusts reached 42 km/h at the time of the wind annotation (9 August, 03:55 UTC) and 56–59 km/h later that morning. The strongest gust of the record, 78 km/h, occurred on 12 August at 11:00 UTC and was not accompanied by a comparable disturbance in V_7.

3.7 Fast fluctuations and an instrumental line

At faster scales, all channels shared a narrow spectral line. Above $\sim 10^{-2}$ Hz, the PSDs showed a peak at 0.108 Hz, corresponding to 9.25 s [Fig. 6(b)]. Band-limited r.m.s. amplitudes over 0.05–0.2 Hz were 0.17–1.47 mV. The peak had the same shape across channels. Interchannel coherence was modest: 0.32–0.33 at the peak, compared with approximately 0.18 nearby.

We provisionally attribute this line to instrumental or environmental interference. Beating between mains interference and the logger conversion cycle is one

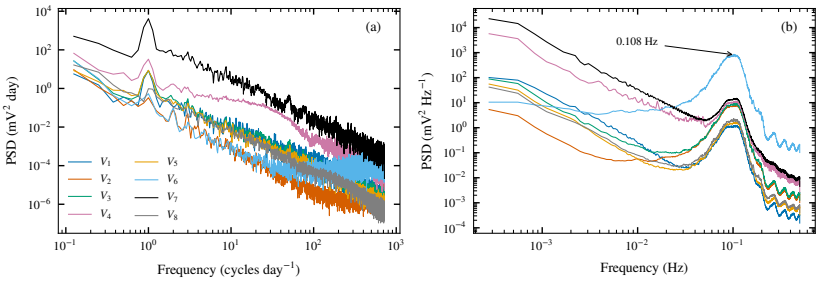


Fig. 6 Power spectral densities of the settled period. (a) Low-frequency band from 1-min means (8-day Welch segments), showing the 1 cycle day^{-1} peak. (b) High-frequency band from the 1-s data (1-h segments), showing the common 0.108 Hz line.

possible source. Its origin was not tested independently. The 0.03 Hz low-pass filter removed it before step detection. Below the line, the spectra followed $f^{-\beta}$, with channel-dependent exponents.

3.8 Impedance spectroscopy

Subsequent EIS measurements characterized the Au–tissue system. Impedance decreased from 0.75 MΩ at 0.1 Hz to 4.2 kΩ at 100 kHz [Fig. 7(a)]. Between 3 and 100 kHz, the reported phase remained near 53°–67° [Fig. 7(b)]. This is consistent with a dispersive CPE response. Below approximately 100 Hz, the phase fell to 5°–20°. The rise in $|Z|$ below 10 Hz indicates increasing electrode polarization.

The 100-mV spectrum had a higher signal-to-noise ratio than the 10-mV spectrum. Fitting its 43 retained points with Eq. (2) gave $R_1 = 270\,\mathrm{k\Omega}$ (±4%), $Q_1 = 1.06 \times 10^{-8}\,\mathrm{S\,s}^n$ (±17%), $n_1 = 0.819 \pm 0.019$, $Q_2 = 2.57 \times 10^{-6}\,\mathrm{S\,s}^n$ (±6%), $n_2 = 0.386 \pm 0.008$, with r.m.s. residuals of 7.8% in $|Z|$ and 4.4° in phase. Equation (3) gave $C_{\mathrm{eff}} = 2.9\,\mathrm{nF}$ and $f_c = 204\,\mathrm{Hz}$. The low exponent, $n_2 \approx 0.39$, indicates a strongly distributed interface. A diffusion-related contribution is possible, although the exponent differs from the ideal diffusion value of 0.5.

Excitation amplitude affected the low-frequency response. At 100 kHz, 10- and 100-mV excitation gave similar impedances of 4.0 and 4.2 kΩ. At 0.1 Hz, the corresponding values were 354 kΩ and 755 kΩ. This difference is consistent with nonlinearity, although the 10-mV spectrum was noisier. Its fit was less well determined, with $R_1 = 171\,\mathrm{k\Omega}$ and n_1 at its upper bound.

DC bias had a smaller effect at high frequency. Across 0.1–1.1 V, $|Z|$ remained within 3.7–4.3 kΩ at 100 kHz [Fig. 7(c)]. At 0.1 Hz, it varied between 414 and 571 kΩ, without a monotonic trend.

3.9 Voltammetry

Voltammetry probed the same system at slower time scales. The CV curves were nearly linear within ±1 V [Fig. 8(a)]. They showed small hysteresis and no resolved faradaic peaks. Over 20 cycles, the chord resistance decreased from 812 kΩ to 717 kΩ. These values are close to the low-frequency impedance of 0.75 MΩ at 0.1 Hz. The zero-current

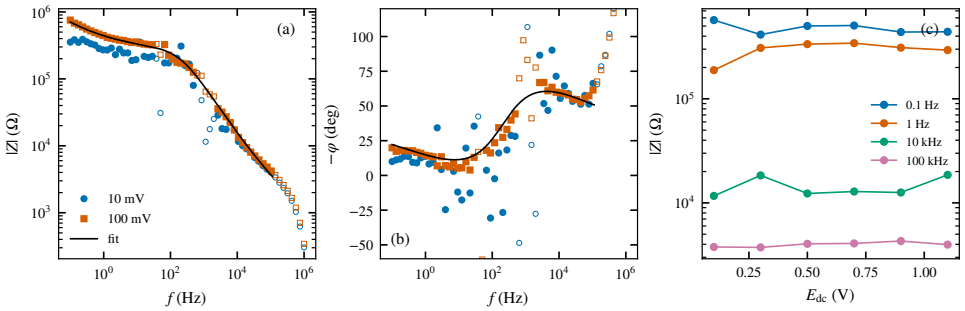


Fig. 7 Potentiostatic EIS at $E_{\mathrm{dc}} = 0.1\,\mathrm{V}$. (a) Magnitude and (b) phase for 10-mV and 100-mV excitation. Filled symbols were used in the fit; open symbols were excluded (mains band and range-switching region). Solid line: fit of Eq. (2) to the 100-mV spectrum. (c) $|Z|$ at four frequencies as a function of DC bias.

potential shifted from −0.650 to −0.377 V. The hysteresis capacitance decreased from 9.9 to 7.4 µF.

Current at $E = 0$ decreased from 0.80 to 0.53 µA. The electrode set therefore behaved as a weak galvanic cell. The configuration combined Au and Pt/Ir electrodes, so part of the offset may come from the different electrode metals. Asymmetric tissue chemistry at the contacts, such as local pH, ion concentration and contact area, may also contribute. The measured capacitance was three orders of magnitude larger than C_{eff}. It is consistent with the low-frequency element (Q_2, n_2) and electrode–tissue double-layer charging.

DPV revealed a bias-dependent change in conductance [Fig. 8(b)]. Differential current was nearly independent of E within $|E| \lesssim 1.8\,\mathrm{V}$. It increased at approximately −1.8 to −2.1 V and +1.95 to +2.2 V for every pulse amplitude. Within each potential window, ΔI was proportional to ΔE_{p} [Fig. 8(c)]. The response was therefore approximately ohmic within each regime. The slopes gave 447 kΩ at $|E| < 1.5\,\mathrm{V}$ ($r^2 = 0.984$), 292 kΩ in the cathodic window ($r^2 = 0.9985$) and 255 kΩ in the anodic window ($r^2 = 0.9990$).

These values connect the DPV and EIS results. The low-bias resistance agrees with $|Z| = 444\,\mathrm{k\Omega}$ at 1 Hz. The high-bias values approach $R_1 = 270\,\mathrm{k\Omega}$. This suggests that electrode reactions reduce the polarization contribution beyond $|E| \approx 2\,\mathrm{V}$. Water electrolysis is one possible mechanism. Its thermodynamic voltage is 1.23 V, while electrode overpotentials could raise the observed onset towards 2 V. The reaction products were not measured, so this assignment remains provisional.

3.10 Galvanostatic impedance tracking at 1 kHz

GEIS assessed short-term stability at 1 kHz. During 5.56 h at night, median $|Z|$ was 21.9 kΩ [Fig. 9(a)]. The interquartile range was 17.1–27.0 kΩ. Ten-minute medians remained within 19.1–24.3 kΩ. No significant trend was detected (−96 Ω/h, $p = 0.52$).

The phase distribution was bimodal [Fig. 9(b)]. Of the points, 61% lay near +71°, assigned as capacitive, and 32% near −90°. Both groups had similar impedance magnitudes: 22.4 and 22.9 kΩ. We provisionally assign the second mode to phase-detection

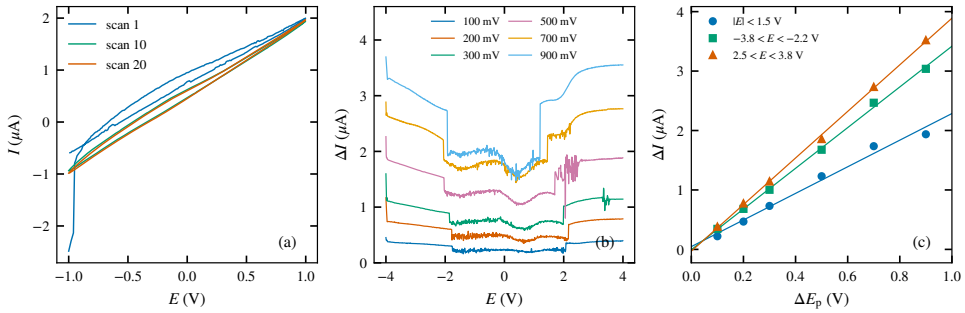


Fig. 8 (a) Cyclic voltammograms (10 mV/s, cycles 1, 10, 20). (b) Differential pulse voltammograms for pulse amplitudes 0.1–0.9 V. (c) Median differential current in three potential windows against pulse amplitude, with linear fits; slopes correspond to 447, 292 and 255 kΩ.

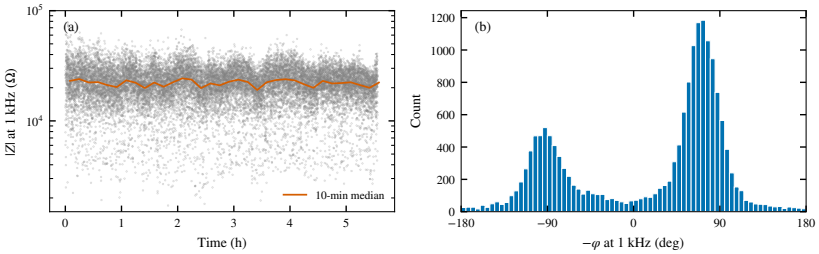


Fig. 9 Galvanostatic impedance at 1 kHz over 5.56 h (31 Aug., from 19:25 UTC). (a) All 17 025 points (grey) and 10-min medians. (b) Phase histogram, showing a capacitive mode near +71° and a spurious mode near −90°.

error at low excitation current. It does not provide secure evidence of inductive behaviour. For the capacitive group, $C = 1/(\omega|Z|\sin|\varphi|)$ gave 7.8 nF, with an IQR of 6.6–9.5 nF. This is of the same order as C_{eff} from EIS.

The excitation conditions limit that comparison. The AC voltage reached 0.68–1.07 V, well above the small-signal regime. The quasi-open-circuit DC potential varied from −3.3 to 4.9 V. These values indicate strongly polarized, nonlinear contacts. They may explain why GEIS gave a lower impedance than the potentiostatic model at 1 kHz (78 kΩ). GEIS is therefore interpreted as a stability record rather than a source of absolute circuit parameters.

3.11 Leaf surface morphology

Surface imaging provided structural context for the electrical measurements. Figure 10 compares uncoated [(a)–(d)] and Au-coated [(e)–(h)] specimens. The coated epidermis showed elongated polygonal cells arranged along the leaf axis [Fig. 10(e)]. Cells were approximately 100–150 µm long and 50–70 µm wide. Stomata were scattered between the cells, with pores parallel to the cell rows. We counted 9 stomata in a 1.00 mm × 0.67 mm field. The estimated density was therefore approximately 13/mm^2. This single-field estimate is indicative.

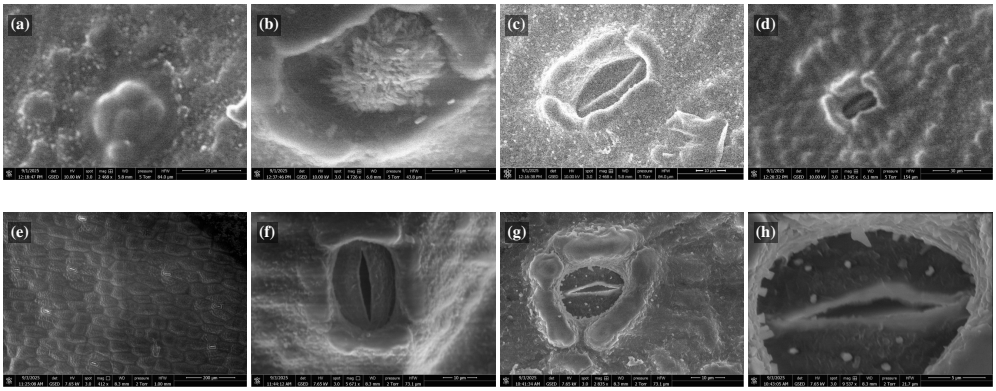


Fig. 10 Environmental SEM images of the *Aloe vera* leaf surface, acquired with GSED. Top row: uncoated specimens, imaged on 1 September 2025 at 10 kV and 5 Torr. Panels show (a) cuticular domes, (b) a depression with a fibrous/crystalline deposit and (c,d) sunken stomata. Bottom row: Au-coated specimens, imaged on 3 September 2025 at 7.65 kV and 2 Torr. Panels show (e) elongated epidermal cells and scattered stomata, (f) a single stoma, (g) a sunken stoma bordered by subsidiary cells and (h) wax-like platelets lining a stomatal pit. The field width in (e) is 1.00 mm. Instrument data and scale bars are retained.

The stomata were sunken. Each guard-cell pair lay within a pit bordered by four raised subsidiary cells [Fig. 10(g)]. The pit opening was approximately 19 µm across. The guard-cell complex measured approximately 27×19 µm. Pore slits reached approximately 21 µm in length and were less than 3 µm wide [Figs. 10(f) and 10(g)]. At higher magnification, platelet-like structures lined the pit rim [Fig. 10(h)]. Their size was approximately 1 µm, consistent with epicuticular wax. Spherical particles of 0.4–0.7 µm occurred inside the pit. Sputtered Au grains were not resolved at these magnifications.

Uncoated specimens showed similar features, with lower contrast and more noise [Figs. 10(a)–10(d)]. The cuticle contained dome-shaped bulges of approximately 25 µm [Fig. 10(a)]. Depressions of approximately 30 µm contained fibrous or crystalline deposits about 20 µm across [Fig. 10(b)]. Sunken, slit-shaped pores were 20–25 µm long [Figs. 10(c) and 10(d)]. Imaging occurred during the day at 2–5 Torr, with partial specimen dehydration. Pore apertures therefore cannot be interpreted as the undisturbed physiological stomatal state.

3.12 Stomatal density and spike timing

The high-vacuum image of an Au-coated leaf [Fig. 11(a)] covers 1.54 mm^2 and shows the ridged epidermis with stomata arranged in files along the leaf axis. Of 41 candidates, 36 were accepted as stomata. The density was 23.3/mm^2 (95% CI 16.4–32.3). This is higher than, but statistically compatible with, the single smaller field of Fig. 10(e) (13.5/mm^2, CI 6.2–25.6) [Fig. 11(b)]. Pooling both fields gives 20.4/mm^2 (CI 14.9–27.3) over 2.21 mm^2. The dark pit apertures measured 22.5 ± 4.2 µm along and 16.4 ± 4.6 µm across their long axis, and 86% were elongated parallel to the leaf axis. The mean nearest-neighbour distance was 124±49 µm [Fig. 11(c)], against 112 µm

expected for a random pattern after edge correction ($R = 1.11$, $z = 1.2$). The stomata are therefore spread approximately at random, with at most a weak tendency to regular spacing.

The density cannot be compared channel by channel with the step events, because stomata were not counted at the electrode sites. Instead, we tested whether the events coincided with the phase in which the stomata are expected to be open. Night covered 41.5% of the settled record. Of the 107 step events on V_7, 85 (79%) occurred at night (binomial $p = 1.6 \times 10^{-15}$), including 78 of the 89 negative events ($p = 3.1 \times 10^{-19}$). The negative events followed sunset with a median delay of 2.6 h (IQR 1.1–4.8 h) [Fig. 11(d)]. Night clustering was weaker but significant on V_4 (22 of 35 events, $p = 0.015$) and V_6 (23 of 33, $p = 0.0013$).

The number of V_7 events per night ranged from 0 to 13 (mean 2.8). It increased with mean night air temperature [Fig. 11(e); Spearman $\rho = 0.61$, $p < 0.001$; negative-binomial incidence-rate ratio 1.24 per K, $p < 0.001$]. It also increased with night VPD ($\rho = 0.41$, $p = 0.026$; ratio 1.71 per kPa, $p = 0.002$) and tended to decrease with night RH ($\rho = -0.32$, $p = 0.08$). Without the two most active nights (26 July and 10 August, 12 and 13 events), the temperature relation remained ($\rho = 0.53$, $p = 0.003$), but the VPD relation did not ($\rho = 0.27$, $p = 0.16$). The spikes are therefore concentrated in the stomatal-opening phase and are most frequent on warm nights.

3.13 Boolean-logic analysis

Threshold switch. The DPV nonlinearity permits a binary description. When plotted against the pulse-top potential, $E + \Delta E_{\mathrm{p}}$, all six curves approached a common step [Fig. 12(a)]. Positive thresholds were 2.11–2.37 V, with little dependence on pulse amplitude. Cathodic thresholds ranged from −1.76 to −2.06 V. The ON/OFF current ratio was modest, at 1.47–1.73. The levels were nevertheless well separated ($d' = 4.6$–8.0). Midpoint classification was 100% correct for $\Delta E_{\mathrm{p}} \leq 0.5$ V. Accuracy was 99.1% at 0.7 V and 94.6% at 0.9 V. The Au–tissue system thus behaved as an approximately symmetric threshold element near 2.2 V. An inverter based on this response and a series load would require circuit-level validation.

Memory. The CV response places a separate limit on logic interpretations. The loops were not pinched at the origin. Apart from one crossing at −0.86 V in cycle 1, the branches did not cross within ±0.9 V. Loop area stabilized near 0.20 µW (µA V) after the first few cycles. Hysteresis width was 7–10% of the current span. These features are consistent with predominantly capacitive memory from double-layer charging. They do not establish an ideal memristor. At 10 mV/s, the data therefore do not support a stateful material-implication logic scheme [19].

Gates between channels. We next examined spontaneous activity through Boolean descriptions (Table 2; Fig. 12(c)). Four outputs, V_3, V_4, V_5 and V_7, exceeded the circular-shift null ($p \leq 0.001$). Each relation involved V_7 or the day/night proxy L. Most added little to a single-input description. For example, $V_3 = \mathrm{COPY}(V_7)$ gave 79.6% accuracy and $V_5 = \mathrm{NOT}(V_7)$ gave 85.6%. For V_4, $\mathrm{NAND}(L, V_7)$ gave 83.3%, compared with 82.8% for NOT V_7.

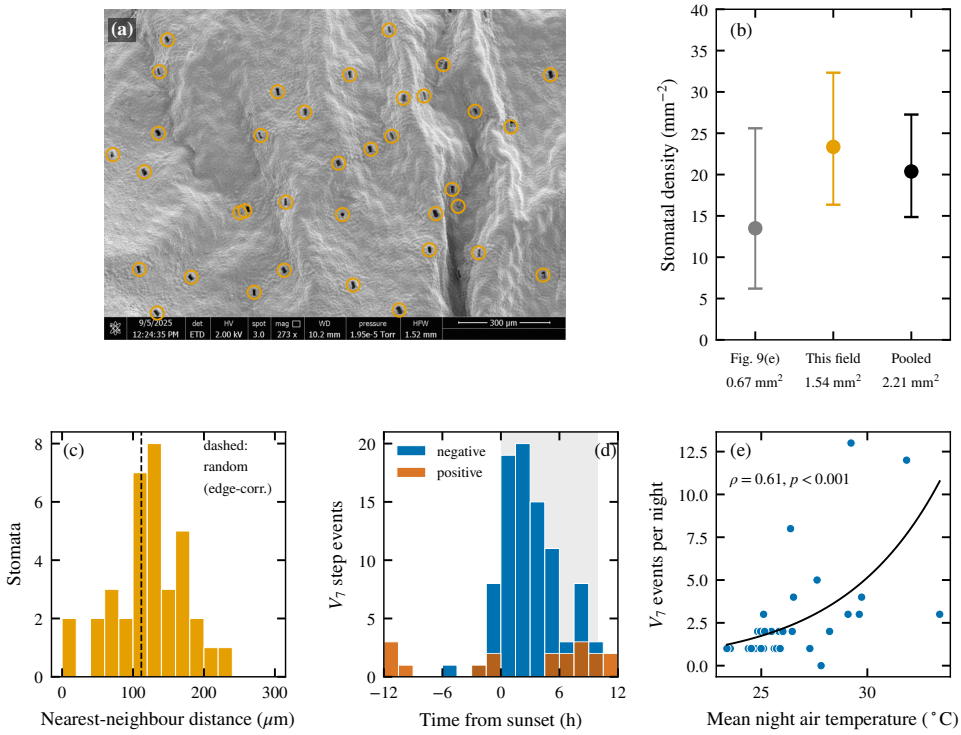


Fig. 11 Stomata and spike timing. (a) Au-coated leaf surface imaged in high vacuum (ETD, 2.00 kV, 5 September 2025; field width 1.52 mm); circles mark the 36 accepted stomata. (b) Stomatal density with 95% Poisson intervals for the field of Fig. 10(e), the field in (a) and both pooled. (c) Nearest-neighbour distances; dashed line, edge-corrected expectation for a random pattern. (d) V_7 step events relative to sunset (settled period); grey band, mean night. (e) V_7 events per night against mean night air temperature, with a negative-binomial fit.

The clearest improvement from a second input occurred for

$$V_7 = L \text{ AND NOT } V_5, \tag{4}$$

with 88.9% accuracy. Accuracy was 86.1% for L alone. The null's 95th percentile was 87.3%, and the circular-shift test gave $p < 0.001$. The truth table shows how V_5 modifies this description [Fig. 12(b)]. During $L = 1$ bins, V_7 was high in 92% of cases when V_5 was low. This fraction fell to 39% when V_5 was high. During $L = 0$ bins with high V_5, it was only 2%. Thus, V_5 acted as a statistical veto within the Boolean description. The observational data do not establish physiological inhibition. Channels V_1, V_2, V_6 and V_8 did not exceed the null.

We repeated the V_7 search with day/night inputs that do not depend on V_7. With radiation, temperature or RH as the input, the best description was $V_7 = \text{NOT}\, V_5$ (85.6%) in every case. Radiation alone gave 75.4%, temperature 84.2% and RH 81.3%. None of these improved on the single-input description, and none exceeded the shift

Table 2 Best Boolean description of each binarized channel (10-min bins, settled period). Acc.$_1$: best single input; Acc.$_2$: best two-input gate; null: 95th percentile of the shift null; p: permutation p value (1000 shifts).

Out	Best gate	Acc.$_1$	Acc.$_2$	null	p
V_1	NOT V_2 AND V_6	0.608	0.620	0.642	0.17
V_2	NAND(V_1,V_6)	0.566	0.574	0.645	0.48
V_3	COPY V_7	0.796	0.796	0.723	< 0.001
V_4	NAND(L,V_7)	0.828	0.833	0.808	< 0.001
V_5	NOT V_7	0.856	0.856	0.821	< 0.001
V_6	NOT L	0.715	0.715	0.733	0.20
V_7	L AND NOT V_5	0.861	0.889	0.873	< 0.001
V_8	COPY V_5	0.572	0.572	0.701	0.83

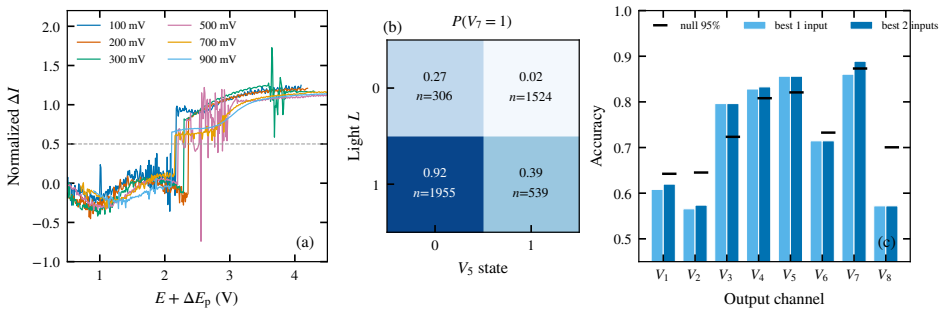


Fig. 12 Boolean-logic analysis. (a) Positive-branch DPV curves, normalized between OFF and ON levels. Curves are plotted against the pulse-top potential, $E + \Delta E_p$. All amplitudes switch near 2.2 V. (b) Truth table for V_7 against the day/night proxy L and V_5. Cells show the probability of high V_7 and the number of 10-min bins. (c) Accuracy of the best single-input and two-input descriptions. Bars above the black marks exceed the shift null's 95th percentile.

null as a two-input gate (radiation $p = 0.19$, temperature $p = 0.15$). The AND NOT relation of Eq. (4) therefore depends on the V_7-derived proxy. The robust result is the antiphase coupling between V_7 and V_5.

4 Discussion

Origin of the diurnal rhythm. The recording separates a daily waveform from slower baseline changes. On V_7, the waveform rose in the morning and fell in the evening. The outdoor weather data refine this picture. The morning rise coincided with sunrise-driven warming, and the mean profile followed air temperature and RH more closely than radiation. The evening decline, however, lagged air temperature by about 2.5 h. An indoor thermal or hydraulic lag, slow relaxation after light-off, or the CAM transition to nocturnal stomatal opening could each produce this delay. Because the hour-to-hour weather anomalies did not drive the signal, V_7 behaves like a stable daily programme rather than a direct thermometer. The smaller amplitude on hot, dry days,

caused by a higher night plateau, is consistent with reduced nocturnal CAM activity under water stress [7], although indoor conditions would be needed to test this.

This daily structure is consistent with previous day/night differences in *Aloe* leaf resistance and capacitor discharge [9]. It is also compatible with CAM physiology. Nocturnal malate accumulation and daytime decarboxylation alter vacuolar proton and ion fluxes [7]. Opposite polarities on V_4 and V_5 need not imply separate rhythmic sources. In differential recordings, electrode orientation can reverse the polarity of a shared source. Controlled light and temperature conditions, with sensors at the plant, are required to distinguish an endogenous circadian component from direct light or thermal responses. Constant-light or constant-darkness recordings would test this distinction.

Slow components and phototropic reorientation. The baseline drift was distinct from the daily rhythm. Over 28 days, the fitted V_7 shift was approximately 146 mV, while daily amplitude remained stable. Channel V_6 showed a separate 25 mV logistic transition centred on 8 August. Both occurred while the plant visibly turned and grew towards the window. Outdoor temperature and humidity showed no matching trend, so seasonal weather is unlikely to explain the steady V_7 drift.

Three explanations may contribute. First, bending and growth can alter strain and contact area at inserted electrodes. A changing junction potential could then shift the baseline without changing the rhythmic component. Second, growth may alter apoplastic pH and membrane potential along the bending leaf. Auxin-dependent proton extrusion provides a physiological route for such changes [13, 14]. Third, reorientation changes the illumination geometry at the electrode sites.

The single logistic transition on V_6, with a width of 1.3 d, is compatible with a mechanical rearrangement. A leaf changing position or moving across an electrode site could produce such a transition. Its shape does not identify the mechanism. Its timing at the onset of a warm, dry spell also suggests a possible change in leaf water status. The link to phototropism remains correlative because bending was assessed visually, without time-resolved angle measurements. Synchronized time-lapse imaging would resolve the relation between movement and potential. A non-moving control plant and substrate reference electrodes would help separate physiological signals from contact changes.

Passive electrical properties. Electrochemical measurements constrain the interpretation of the plant–electrode interface. EIS gave $R_1 = 270\,\mathrm{k\Omega}$, close to the high-bias DPV range of 255–292 kΩ. Low-bias DPV gave 447 kΩ, compared with $|Z|(1\,\mathrm{Hz}) = 444\,\mathrm{k\Omega}$. CV gave 717–812 kΩ, compared with $|Z|(0.1\,\mathrm{Hz}) = 755\,\mathrm{k\Omega}$. The agreement is therefore conditional on bias and time scale. A single "DC resistance" cannot describe the full response.

The equivalent circuit accounts for this dependence through electrode polarization. Its contribution increases at low frequency and appears to decrease above $|E| \approx 2\,\mathrm{V}$. The tissue-associated CPE had $n_1 = 0.82$, a capacitance of a few nanofarads and $f_c \approx 200\,\mathrm{Hz}$. These values are consistent with distributed membrane capacitance and β-dispersion [11, 12]. The low-frequency nonlinearity also accords with previous reports of nonlinear electrical behaviour in *Aloe* [8, 10]. However, the present CV loops do not independently establish memristance.

Leaf morphology provides a possible structural contribution to the high impedance. SEM showed a continuous cuticle, wax-like surface structures and sparse sunken stomata. These features are typical of CAM succulents [7] and may restrict electrical access from surface contacts. Their contribution depends on electrode placement and penetration, which remain incompletely documented. Morphology alone therefore cannot determine the effective contact area.

Spikes and stomata. The step events cluster where stomatal activity is expected in a CAM plant: after sunset and during the first half of the night, when stomata open and CO_2 is fixed into malate [7]. Their higher frequency on warm nights is consistent with a link to water and gas-exchange stress, because warm, dry nights raise transpirational demand while stomata are open. The same nights produced the higher night plateau and smaller daily amplitude of V_7 described above. This is a temporal association only. Ion fluxes in guard cells, the vacuolar malate cycle and the evening fall of temperature all share this timing. With about 20 stomata per mm^2, an inserted wire or printed electrode of sub-millimetre size contacts only a few stomatal complexes, so a direct test needs stomatal counts at each electrode site, porometry or gas-exchange measurements at night, and recordings with stomata closed chemically or by high humidity.

Toward unconventional computing. The threshold response and Boolean relations suggest experiments in plant-based computation. The Au–tissue system switched near 2.2 V. Spontaneous signals also followed the relation $V_7 = L$ AND NOT V_5 [Eq. (4)]. These observations provide a comparison with logic gates reported in plant roots [20]. They do not yet demonstrate computation under controlled inputs.

The main limitation is that L was derived from the mean profile of V_7. Its predictive accuracy is therefore partly circular. With independent radiation, temperature or humidity inputs, the AND NOT relation disappeared and only the antiphase coupling NOT V_5 remained. Most other significant relations reduced to COPY or NOT of the shared daily state. Common environmental forcing could generate such dependencies without signal processing between channels.

A direct test requires independently controlled inputs. Candidate inputs include two switched voltage pulses at 0 or 2.5 V, above the observed 2.2 V threshold, or two light sources. All four input combinations should be applied in randomized order with replicates. Outputs could then be recorded on the Pt/Ir channels. This would permit a full truth table with error rates, switching times and energy per operation. Voltage-driven tests would also need to separate tissue responses from electrode reactions.

Limitations. The study concerns one plant without biological replicates. Light and temperature were uncontrolled. Weather was available only as outdoor reanalysis, not as indoor measurements at the plant. Electrochemical measurements followed the potential recording by 11–12 days and used a separate three-electrode set with printed Au electrodes. The fitted parameters describe that system and cannot be assigned directly to the differential Pt/Ir channels. SEM covered a few fields on two specimens. Tests on daily quantities, including drift regressions, treated days as independent. Their significance should therefore be interpreted descriptively.

5 Conclusions

Continuous recording resolved electrical activity across several time scales in one *Aloe vera* plant. After approximately one week of electrode settling, all eight channels showed a daily rhythm. The largest spanned 65 mV, with morning and evening half-amplitude crossings at 06:15 and 20:00 UTC. Abrupt steps contributed to the evening decline. Of 107 detected events on V_7, 89 were negative and occurred mainly between 15:00 and 03:00 UTC.

Slower changes coexisted with this daily activity. Channel V_7 drifted at 5.2 mV/d without a change in daily amplitude. Channel V_6 underwent a 25 mV logistic transition with a width of 1.3 d. Both changes coincided with visible growth and reorientation towards the window. Their relation to phototropism remains correlative. Outdoor weather showed no matching trend. The daily V_7 waveform was in phase with air temperature in the morning but lagged it by about 2.5 h in the evening, and its amplitude decreased on hot, dry days through a higher night level.

Subsequent electrochemical measurements separated tissue-associated resistance from interfacial polarization. The fitted circuit contained $R_1 = 270\,\mathrm{k\Omega}$ in parallel with a CPE. This element had $n_1 = 0.82$, $C_{\mathrm{eff}} = 2.9\,\mathrm{nF}$ and $f_{\mathrm{c}} = 204\,\mathrm{Hz}$. A second, series CPE described polarization, with $n_2 = 0.39$. DPV and CV gave consistent resistance estimates at corresponding bias and time scales.

The Au–tissue system also showed a threshold near 2.2 V. Binarized activity was best described by $V_7 = L$ AND NOT V_5, with L derived from the daily V_7 profile. With independent weather inputs, it reduced to $V_7 = \mathrm{NOT}\, V_5$. This motivates controlled-input tests but does not establish a causal gate. The present record shows that 1-s sampling can resolve abrupt events alongside multi-week drift. Synchronized imaging and environmental measurements are the next step towards linking those signals to slow plant movement.

Acknowledgements. We thank David Paton for scanning electron microscopy imaging.

Declarations

Conflict of Interest. The authors have no conflicts to disclose.

Data Availability. The data that support the findings of this study are available from the corresponding author upon reasonable request.

References

[1] A. G. Volkov (ed.), *Plant Electrophysiology: Theory and Methods* (Springer, Berlin, 2006).

[2] J. Fromm and S. Lautner, "Electrical signals and their physiological significance in plants," Plant Cell Environ. **30**, 249–257 (2007).

[3] A. Gallé, S. Lautner, J. Flexas, and J. Fromm, "Environmental stimuli and physiological responses: The current view on electrical signalling," Environ. Exp. Bot. **114**, 15–21 (2015).

[4] V. Sukhov, "Electrical signals as mechanism of photosynthesis regulation in plants," Photosynth. Res. **130**, 373–387 (2016).

[5] A. G. Volkov and D. R. A. Ranatunga, "Plants as environmental biosensors," Plant Signal. Behav. **1**, 105–115 (2006).

[6] S. K. Chatterjee, S. Das, K. Maharatna, E. Masi, L. Santopolo, S. Mancuso, and A. Vitaletti, "Exploring strategies for classification of external stimuli using statistical features of the plant electrical response," J. R. Soc. Interface **12**, 20141225 (2015).

[7] U. Lüttge, "Ecophysiology of crassulacean acid metabolism (CAM)," Ann. Bot. **93**, 629–652 (2004).

[8] A. G. Volkov, J. C. Foster, E. Jovanov, and V. S. Markin, "Anisotropy and nonlinear properties of electrochemical circuits in leaves of *Aloe vera* L.," Bioelectrochemistry **81**, 4–9 (2011).

[9] A. G. Volkov, K. Baker, J. C. Foster, J. Clemmons, E. Jovanov, and V. S. Markin, "Circadian variations in biologically closed electrochemical circuits in *Aloe vera* and *Mimosa pudica*," Bioelectrochemistry **81**, 39–45 (2011).

[10] A. G. Volkov, C. Tucket, J. Reedus, M. I. Volkova, V. S. Markin, and L. Chua, "Memristors in the electrical network of *Aloe vera* L.," Plant Signal. Behav. **9**, e29056 (2014).

[11] M. I. N. Zhang and J. H. M. Willison, "Electrical impedance analysis in plant tissues: A double shell model," J. Exp. Bot. **42**, 1465–1475 (1991).

[12] I. Jócsák, G. Végvári, and E. Vozáry, "Electrical impedance measurement on plants: A review with some insights to other fields," Theor. Exp. Plant Physiol. **31**, 359–375 (2019).

[13] J. M. Christie, "Phototropin blue-light receptors," Annu. Rev. Plant Biol. **58**, 21–45 (2007).

[14] E. Liscum, S. K. Askinosie, D. L. Leuchtman, J. Morrow, K. T. Willenburg, and D. R. Coats, "Phototropism: Growing towards an understanding of plant movement," Plant Cell **26**, 38–55 (2014).

[15] P. D. Welch, "The use of fast Fourier transform for the estimation of power spectra: A method based on time averaging over short, modified periodograms," IEEE Trans. Audio Electroacoust. **15**, 70–73 (1967).

[16] M. E. Orazem and B. Tribollet, *Electrochemical Impedance Spectroscopy* (Wiley, Hoboken, NJ, 2008).

[17] G. J. Brug, A. L. G. van den Eeden, M. Sluyters-Rehbach, and J. H. Sluyters, "The analysis of electrode impedances complicated by the presence of a constant phase element," J. Electroanal. Chem. **176**, 275–295 (1984).

[18] A. J. Bard and L. R. Faulkner, *Electrochemical Methods: Fundamentals and Applications*, 2nd ed. (Wiley, New York, 2001).

[19] J. Borghetti, G. S. Snider, P. J. Kuekes, J. J. Yang, D. R. Stewart, and R. S. Williams, "'Memristive' switches enable 'stateful' logic operations via material implication," Nature **464**, 873–876 (2010).

[20] A. Adamatzky, G. Ch. Sirakoulis, G. J. Martinez, F. Baluška, and S. Mancuso, "On plant roots logical gates," BioSystems **156–157**, 40–45 (2017); arXiv:1610.04602.

[21] H. Hersbach *et al.*, "The ERA5 global reanalysis," Q. J. R. Meteorol. Soc. **146**, 1999–2049 (2020).

[22] P. Zippenfenig, "Open-Meteo.com Weather API," Zenodo (2023), doi:10.5281/zenodo.7970649.

[23] P. J. Clark and F. C. Evans, "Distance to nearest neighbor as a measure of spatial relationships in populations," Ecology **35**, 445–453 (1954).

[24] K. P. Donnelly, "Simulations to determine the variance and edge effect of total nearest-neighbour distance," in *Simulation Methods in Archaeology*, edited by I. Hodder (Cambridge University Press, Cambridge, 1978), pp. 91–95.